Supplemental Material : Magnetic resonance with squeezed microwaves

A. Bienfait[1], P. Campagne-Ibarcq[1], A. H. Kiilerich[2], X. Zhou[1,3], S. Probst[1], J.J. Pla[4], T. Schenkel[5], D. Vion[1], D. Esteve[1], J.J.L. Morton[6], K. Moelmer[2], and P. Bertet[1]

[1]*Quantronics group, SPEC, CEA, CNRS, Université Paris-Saclay, CEA Saclay 91191 Gif-sur-Yvette Cedex, France*

[2]*Department of Physics and Astronomy, Aarhus University, Ny Munkegade 120, DK-8000 Aarhus C, Denmark*

[3]*Institute of Electronics Microelectronics and Nanotechnology, CNRS UMR 8520, ISEN Department, Avenue Poincaré, CS 60069, 59652 Villeneuve d'Ascq Cedex, France*

[4]*School of Electrical Engineering and Telecommunications, University of New South Wales, Anzac Parade, Sydney, NSW 2052, Australia*

[5]*Accelerator Technology and Applied Physics Division, Lawrence Berkeley National Laboratory, Berkeley, California 94720, USA and*

[6] *London Centre for Nanotechnology, University College London, London WC1H 0AH, United Kingdom*

(Dated: May 22, 2017)

CONTENTS

I. Theory details 2

A. Squeezing and amplification by a Josephson parametric amplifier 2

B. Resonator output signal and its fluctuations 3

II. Experimental details 5

A. Measurement setup 5

B. Squeezing-enhanced echo: data acquisition and processing 7

C. Sensitivity estimate and numerical model 8

III. Characterization of the mean number of thermal photons 10

References 17

I. THEORY DETAILS

A. Squeezing and amplification by a Josephson parametric amplifier

In the experiment, we use Josephson parametric amplifiers (JPA) to both produce a squeezed vacuum input field incident on the resonator and to amplify a single quadrature of the emitted radiation in a noiseless manner. For a general review on parametric amplification, see [1]. Here we establish the formalism, focusing on the limit of broad band squeezing.

The transformation of the field quadrature operators by a JPA employed in the degenerate mode is described by an amplitude gain factor G,

$$\begin{aligned} \hat{X}_{\text{out}} &= G\hat{X}_{\text{in}} \\ \hat{Y}_{\text{out}} &= G^{-1}\hat{Y}_{\text{in}}. \end{aligned} \tag{S1}$$

The amplification, that we apply to the output from the ESR resonator, is hence unitary and maintains the signal-to-noise ratio [2]. Equations (S1) are equivalent to a transformation of the field annihilation and creation operators ($\hat{X} = \frac{1}{2}(\hat{a} + \hat{a}^\dagger)$, $\hat{Y} = \frac{1}{2i}(\hat{a} - \hat{a}^\dagger)$),

$$\begin{aligned} \hat{a}_{\text{out}} &= \frac{G + G^{-1}}{2}\hat{a}_{\text{in}} + \frac{G - G^{-1}}{2}\hat{a}_{\text{in}}^\dagger \\ \hat{a}_{\text{out}}^\dagger &= (\hat{a}_{\text{out}})^\dagger. \end{aligned} \tag{S2}$$

Assuming the broadband limit and applying the JPA to a vacuum or a thermal state, Eqs. S2 lead to the temporal correlations of the squeezed output field,

$$\begin{aligned}\langle \hat{a}^\dagger_{\rm out}(t)\hat{a}_{\rm out}(t')\rangle &= \left(\frac{G+G^{-1}}{2}\right)^2 \langle \hat{a}^\dagger_{\rm in}(t)\hat{a}_{\rm in}(t')\rangle + \left(\frac{G-G^{-1}}{2}\right)^2 \langle \hat{a}_{\rm in}(t)\hat{a}^\dagger_{\rm in}(t')\rangle \equiv N\delta(t-t') \\ \langle \hat{a}_{\rm out}(t)\hat{a}_{\rm out}(t')\rangle &= \frac{G+G^{-1}}{2}\frac{G-G^{-1}}{2}\left(\langle \hat{a}^\dagger_{\rm in}(t)\hat{a}_{\rm in}(t')\rangle + \langle \hat{a}_{\rm in}(t)\hat{a}^\dagger_{\rm in}(t')\rangle\right) \equiv M\delta(t-t').\end{aligned} \tag{S3}$$

The action of the JPA is hence characterized by a mean output photon number

$$N = \frac{G^2+G^{-2}}{2}\overline{n} + \frac{G^2+G^{-2}-2}{4}, \tag{S4}$$

where $\overline{n}$ is the input mean photon number ($\mathcal{G} \equiv \frac{G^2+G^{-2}}{2}$ is called the *power gain*). The two-photon coherence,

$$M = \frac{G^2-G^{-2}}{4}(2\overline{n}+1) \tag{S5}$$

characterizes the degree of squeezing by the phase sensitive amplification. In the case of a vacuum input state, the mean output photon number is $N = \frac{G^2+G^{-2}-2}{4}$ and we have $M = \sqrt{N(N+1)}$.

If the JPA driving flux modulation at $2\omega_0$ has a phase 2ϕ, the squeezing occurs for a rotated quadrature component and is represented by a complex value, $M \to Me^{2i\phi}$ in Eq. S3. Using the expressions in Eq. S3, we readily find that a rotated quadrature component $\hat{X}_\theta = \frac{1}{2}(e^{-i\theta}\hat{a}_{\rm out} + e^{i\theta}\hat{a}^\dagger_{\rm out})$ of the squeezed state has a variance,

$$\delta X^2_\theta = \langle \hat{X}^2_\theta\rangle = \frac{1}{2}\left[N + M\cos\left(2(\theta-\phi)\right) + \frac{1}{2}\right]. \tag{S6}$$

The angles $\theta = \phi$ and $\theta = \pi/2 + \phi$ specify the principal axes of the squeezing ellipse, along which the fluctuations are anti-squeezed and squeezed by the phase sensitive gain factors G and G^{-1}, respectively.

In the case of steady state squeezing with a finite bandwidth, Δ_{sq}, the delta-function correlations in Eqs. S3 are replaced by exponential functions in the time argument $|t-t'|$ [1]. In Section II of the main text, the squeezed output field $\hat{a}_{\rm out}$ is taken as the input to the resonator system containing the probed spin ensemble.

B. Resonator output signal and its fluctuations

We now present details of the derivation of the theoretical expressions given in Section II of the main text for the amplitude and noise properties of the cavity output field. We provide

closed-form analytical results in the special case of a Lorentzian spin-frequency distribution uncorrelated with the coupling strengths.

Applying the Fourier transforms, $\tilde{h}(\omega) = \frac{1}{\sqrt{2\pi}} \int h(t) e^{-i\omega t}\, dt$ and $h(t) = \frac{1}{\sqrt{2\pi}} \int \tilde{h}(\omega) e^{i\omega t}\, d\omega$, the equations of motion Eqs. (2, 3) in [3] can be written in algebraic form,

$$\begin{aligned} -i\omega\tilde{a}(\omega) &= -\frac{\kappa}{2}\tilde{a}(\omega) - i\sum_j g_j\tilde{\sigma}_j(\omega) + \sqrt{\kappa_L}\tilde{b}_{\text{loss}}(\omega) + \sqrt{\kappa_C}\tilde{b}_{\text{in}}(\omega) \\ -i\omega\tilde{\sigma}_j(\omega) &= -(\gamma + i\Delta_j)\tilde{\sigma}_j(\omega) - ig_j\tilde{a}(\omega) + \frac{\alpha}{\sqrt{2\pi}} e^{i\Delta_j\tau} + \sqrt{2\gamma}\tilde{F}_j(\omega). \end{aligned} \tag{S7}$$

The equations for the spin operators can be formally solved and subsequently yield the expression for the intra-cavity field operator

$$\tilde{a}(\omega) = \frac{-\frac{i}{\sqrt{2\pi}}\sum_j \alpha g_j e^{i\Delta_j\tau}/(\gamma + i\Delta_j - i\omega) + \tilde{F}_{\text{spin}}(\omega) + \sqrt{\kappa_L}\tilde{b}_{\text{loss}}(\omega) + \sqrt{\kappa_C}\tilde{b}_{\text{in}}(\omega)}{\kappa/2 - i\omega + \sum_j g_j^2/(\gamma + i\Delta_j - i\omega)}. \tag{S8}$$

In this equation,

$$\tilde{F}_{\text{spin}}(\omega) = -i\sqrt{2\gamma}\sum_j g_j \frac{\tilde{F}_j(\omega)}{(\gamma + i\Delta_j - i\omega)} \tag{S9}$$

with $[\tilde{F}_{\text{spin}}(\omega), \tilde{F}^\dagger_{\text{spin}}(\omega')] = 2\gamma\sum_j g_j^2 \frac{\delta(\omega-\omega')}{\gamma^2+(\Delta_j-\omega)^2}$, accounts for the contribution of the spins to the noise in the cavity field.

The output field operator is related to the cavity mode operator by the input-output relation Eq. (4) in [3], which for a cavity field of the form Eq. (S8) allows the relative contributions of the spin ensemble and noise sources to be parametrized by a set of four complex frequency dependent coefficients as given in Eqs. (6-9) in [3]. The result is displayed in Eq. (5) in [3], and we note that the output field is completely determined by the frequency dependent ensemble cooperativity Eq. (10) in [3] and the amplitude factor Eq. (11) in [3]. In the following, we outline how a few realistic assumptions lead to analytic expressions for these quantities.

The spin Larmor frequencies have a given distribution $f(\Delta)$ and with a large number of spins, we may replace the sum over spins in $\tilde{a}(\omega)$ by an integral $\sum_j \cdot \to N_{\text{spins}} \int d\Delta\, f(\Delta)\cdot$. For simplicity, we assume that the variation in the coupling strengths g_j is small and uncorrelated with the frequency distribution, such that we may introduce a mean coupling constant $g = \sqrt{\frac{1}{N_{\text{spins}}}\sum_j |g_j|^2}$. The sum in the denominator of Eq. (S8) can then be written as $\kappa C(\omega)/2$ by introducing the frequency-dependent ensemble cooperativity,

$$C(\omega) = \int \frac{2g^2 N_{\text{spins}} f(\Delta)}{\kappa(\gamma + i\Delta - i\omega)}\, d\Delta. \tag{S10}$$

Likewise, the sum in the numerator can be written as

$$A(\omega) = \int \frac{g\alpha N_{\text{spins}} f(\Delta) e^{i\Delta\tau}}{\gamma + i\Delta - i\omega}\, d\Delta. \tag{S11}$$

Finally, the magnitude of the spin noise contribution $\tilde{F}_{\text{spin}}(\omega)$ in the numerator is similarly assessed by replacing the sum in the commutator relation by an integral yielding $[\tilde{F}_{\text{spin}}(\omega), \tilde{F}^{\dagger}_{\text{spin}}(\omega')] = \kappa \text{Re}\,[C(\omega)]\,\delta(\omega - \omega')$.

From the expressions above, the cooperativity and amplitude factors may be evaluated for any distribution of spin frequencies. As an illustrative example, we consider a Lorentzian lineshape of the spin Larmor frequencies, $f(\Delta) = (\Gamma/2\pi)/(\Delta^2 + \Gamma^2/4)$. The integrals in Eqs. (S10, S11) can then be performed analytically. This yields the frequency dependence of the ensemble cooperativity,

$$C_{\text{Lorentzian}}(\omega) = \frac{2g^2 N_{\text{spins}}[\Gamma/2 + \gamma + i\omega]}{\kappa[(\gamma + \Gamma/2)^2 + \omega^2]}. \tag{S12}$$

The numerator of the integrand in $A(\omega)$ has complex poles at $\Delta = i\Gamma/2 + \omega$ and $\Delta = i\gamma + \omega$. Due to the the exponential factor $e^{-\Gamma\tau/2}$ evaluated at the echo time which occurs much later than $1/\Gamma$, the contribution from the first pole is negligible. The second pole, however, yields the weaker damping factor $e^{-\gamma\tau}$ and a finite contribution,

$$A_{\text{Lorentzian}}(\omega) = (\alpha/\sqrt{2\pi})(N_{\text{spins}}\Gamma/[(i\gamma + \omega)^2 + \Gamma^2/4])e^{-\gamma\tau + i\omega\tau} \tag{S13}$$

with a frequency width $\sim \Gamma/2$.

II. EXPERIMENTAL DETAILS

A. Measurement setup

The detailed microwave setup is shown in Fig. S1. The experiment described in the main text and schematized in Fig. 2c makes use of the green and red lines. They connect successively the SQZ, the ESR resonator coupled at rate κ_C, the AMP, followed by the HEMT and room-temperature amplification. The green input port is used to transmit the spin driving pulses to the ESR resonator. The ESR resonator design and fabrication details are given in [4].

In addition, the setup includes additional input-output lines to probe the LC resonator in reflection on port 1 (blue lines), in transmission (blue-green lines), and in reflection on

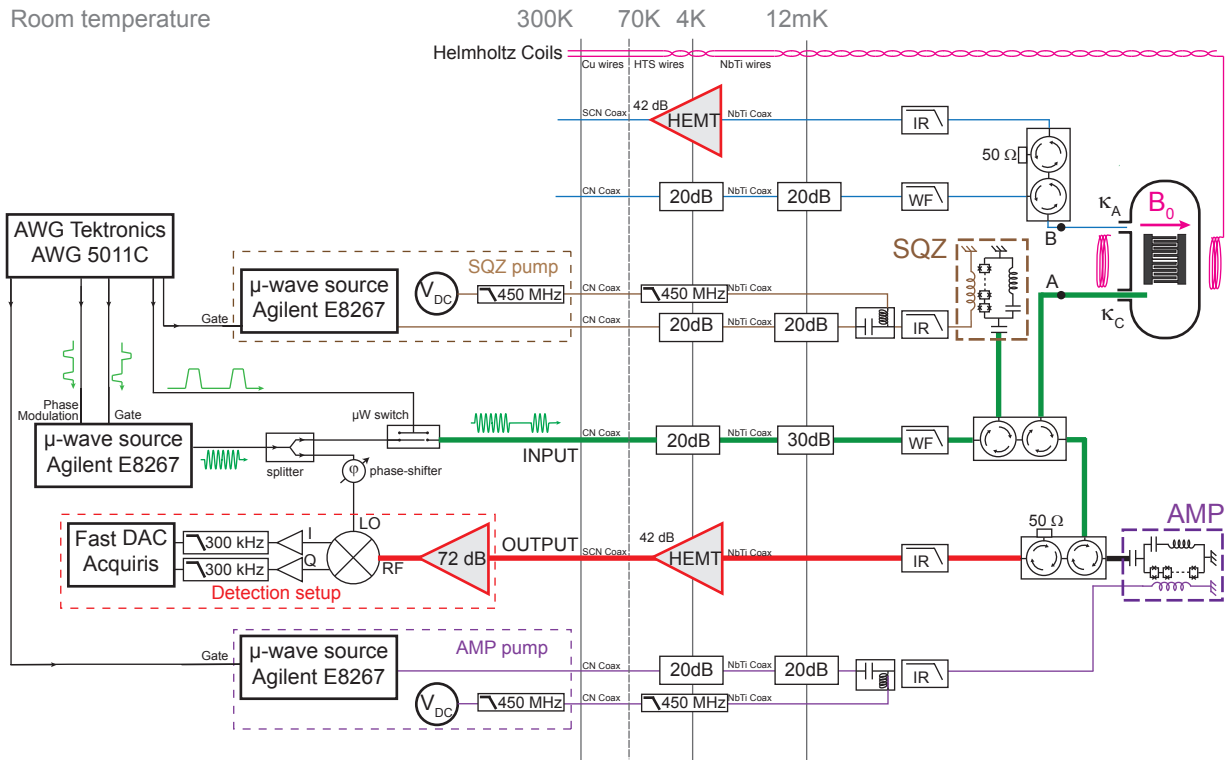

FIG. S1. **Measurement setup**

port 2 (green-red lines). Measurement of the full resonator scattering matrix and a fit to the resonator input-output formulas [5] yields $\kappa_A = 3 \cdot 10^3$ s^{-1}, $\kappa_C = 1.6 \cdot 10^6$ s^{-1} and $\kappa_L = 6 \cdot 10^4$ s^{-1}.

Input lines are isolated from microwave photons emitted from higher temperature stages by a minimum of 20 dB at 4 K and 20 dB at 20 mK, and from infrared photons by commercial absorptive filters (Wavefade FLP0960) anchored at 20 mK. Output lines are protected from microwave noise by a minimum of two circulators and and from infra-red photons by home-made absorptive filters. The ESR resonator and both JPAs are magnetically shielded, see [4] for details.

The generation of the microwave pulses at the input and the detection setup are as described in Ref. [4]. As explained in the main text, AMP and SQZ have the same design [6], and both devices can be tuned to the desired operating frequency via a DC bias of the flux threading their SQUID-array. The two microwave pump tones are generated by microwave sources locked with a 1 GHz synchronization loop to the microwave source providing the excitation pulses and the local-oscillator tone to ensure phase stability. The pump tones are

in addition pulsed via the microwave source internal switches to generate gain only when needed.

B. Squeezing-enhanced echo: data acquisition and processing

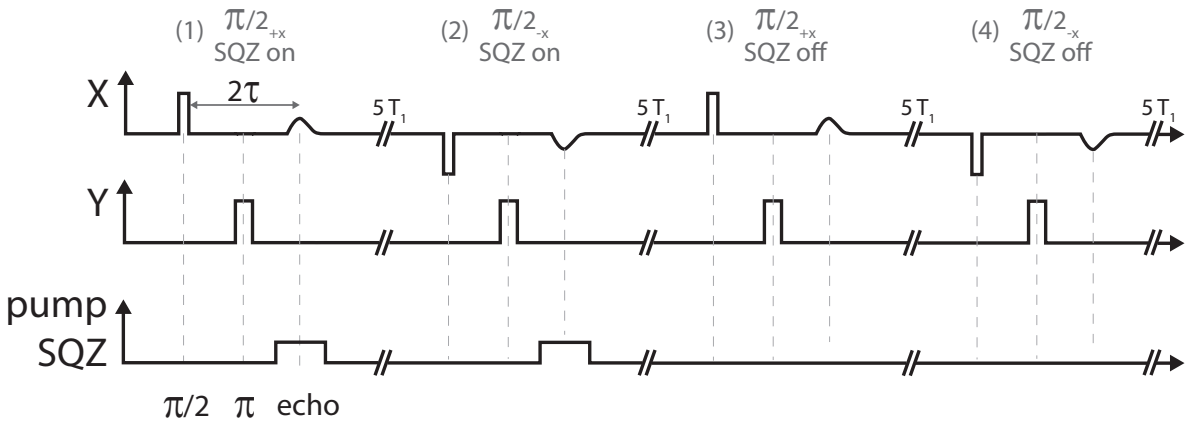

FIG. S2. **Experimental acquisition sequence** taken with $\tau = 200$ µs. Phase cycling as well as alternate SQZ switching are used to compensate setup drifts during the 6 h long acquisiton.

We describe in the following the acquisition and post-processing of the echo data shown in Fig. 5(c and d) of the main text. To minimize setup drifts, we alternate echos acquired with SQZ on and with SQZ off as well as use phase-cycling, as shown in Fig. S2. We acquire $N_{\rm avg} = 2500$ echos with SQZ on and 2500 SQZ off. The quadrature voltage $I(t)$ is digitalized at a sampling rate of 1pt/μs with an acquisition bandwidth of 300 kHz. The data is recorded in a time window $T = 70\,\mu$s centered on the echo. The waiting time between each echo sequence is taken to be $T_{\rm rep} \approx 5T_1 = 5\,$s.

We compute the averaged signals shown in Fig. 5b of the main text as:

$$\bar{I}_{\rm on}(t) = \sum_{i=1}^{N_{\rm avg}} \frac{I_{(1),i}(t) - I_{(2),i}(t)}{2} \text{ and } \bar{I}_{\rm off}(t) = \sum_{i=1}^{N_{\rm avg}} \frac{I_{(3),i}(t) - I_{(4),i}(t)}{2} \tag{S14}$$

where subscripts (i) are denoted in Fig. S2. The noise histograms in Fig. 3c are computed from the bins $\{I_{(1),i}(t) - \bar{I}_{\rm on}(t), \forall i, \forall t\} \cup \{I_{(2),i}(t) + \bar{I}_{\rm on}(t), \forall i, \forall t\}$ when the SQZ is on and $\{I_{(3),i}(t) - \bar{I}_{\rm off}(t), \forall i, \forall t\} \cup \{I_{(4),i}(t) + \bar{I}_{\rm off}(t), \forall i, \forall t\}$. To ensure the echo emission is not affecting the noise properties, we have also computed the noise histograms and variances keeping only identical stamping times t and found no variations.

$u(t)$	Echo shape			Top Hat function		
SQZ	$\langle I \rangle$	$\sqrt{\langle \Delta I^2 \rangle}$	SNR	$\langle I \rangle$	$\sqrt{\langle \Delta I^2 \rangle}$	SNR
OFF	0.179	0.202	0.886	0.161	0.202	0.797
ON	0.177	0.181	0.973	0.160	0.181	0.884
ON/OFF ratio	0.988	0.897	1.10	0.992	0.894	1.11

TABLE S1. **Experimental results**.

To compute the SNR for both echos, we define modes of the propagating field as $\langle O \rangle = \frac{1}{T}\langle O(t) \rangle u(t)dt$ with $u(t)$ a filter function normalized as $\frac{1}{T}\int [u(t)]^2 dt = 1$ [4]. We pick as filter function the echo averaged signal $u(t) \propto [I_{\text{on}}(t) + I_{\text{off}}(t)]/2$. For each echo $\{(n), i\}$, we can thus evaluate the signal and noise quantities as $\langle I_{(n),i} \rangle$ and $\sqrt{\langle \Delta I^2_{(n),i} \rangle}$. Averaging over all recorded echos yields the noise and echo signal shown in Table S1, demonstrating a noise reduction by 11%. Repeating the same procedure for a tophat u function of width 20 µs centered on the echo yields similar results.

C. Sensitivity estimate and numerical model

To estimate the sensitivity of the experiment and its improvement when using squeezed vacuum, we shall determine the number of spins contributing to the echo signal shown in Fig. 5 of the main text. This number is defined as the number of spins excited by the first $\pi/2$ pulse of the Hahn echo sequence. The resonator bandwidth is 20 times smaller than the spin linewidth, broadened due to induced strain, and as in [4] we thus need to resort to numerical simulations. In these simulations, the system is modelled as N_D spin-1/2 systems coupled to the resonator following Eq. (1) in [3]. The evolution of the spin observables and the intra-resonator field mean-values is then found by integrating the master equation of the system with the resonator leakage and the spin decoherence taken into account in a Born-Markov approximation [7]. To describe the inhomogeneity in spin frequencies and coupling constants, the spin ensemble is divided in M sub-ensembles with coupling constants $g^{(m)}$ and detunings from the resonator frequency $\Delta^{(m)}$.

In our former work [4], using the same sample and a resonator of similar geometry, additional measurements such as the absorption of a weak microwave pulse and Rabi oscillations allowed us to determine the spin distribution at $B_0 = 2.8$ mT (peak of the line)

to be well modelled by a Gaussian distribution in g of central value $g_0/2\pi = 56$ Hz and FWHM $\Delta g = 1.5$ Hz and a square distribution for the spin detunings Δ with a width far exceeding the resonator bandwidth. Both distributions were weighted with a total overall factor $N_D = 3.6 \times 10^5$. Compared to [4], the resonator presented in the main text has a 10 times lower quality factor, corresponding to a 10 times larger linewidth and damping rate. Repeating the numerical simulations of [4], taking into account these modifications, we characterize the number of spins contributing to the signal from the $B_0 = 2.8$ mT peak to be $N_{\text{spins}} = 1.2 \times 10^5$.

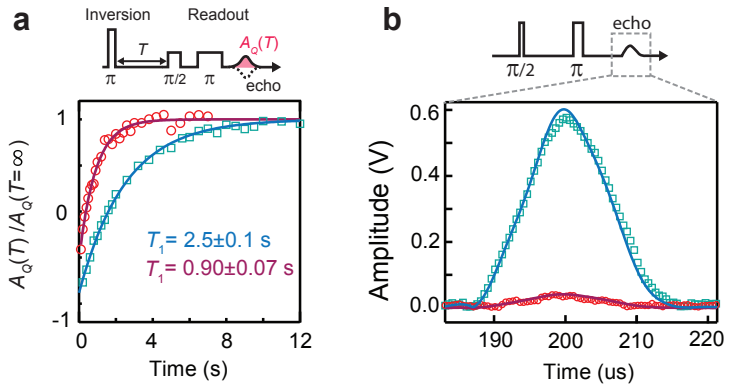

FIG. S3. **Calibration of number of excited spins.** In both panels, data acquired at $B_0 = 2.6$ mT ($B_0 = 2.8$ mT) are represented by red circles (blue squares) **a** Spin relaxation times measured using inversion recovery, well fit by exponential decays (solid lines). **b** Echo time traces reproduced via numerical simulations (solid lines).

We now need to characterize the number of spins at the magnetic field used in the main text, $B_0 = 2.6$ mT. We would like to proceed by comparing the echo amplitudes recorded at $B_0 = 2.6$ mT and $B_0 = 2.8$ mT. We find experimentally a ratio $\alpha \approx \times 25$. However, a direct comparison is not possible since these two spin subsets can not be modelled by the same coupling constant distribution. Indeed, the spin resonance frequency distribution is caused by strain applied by thermal contraction of the aluminium on the silicon substrate. As a result, the spin spectral and spatial distributions are linked [8]. Spins on the low-field side of the peak at $B_0 = 2.6$ mT correspond to spins lying near the edge of the aluminium wire, whereas spins contributing to the $B_0 = 2.8$ mT peak correspond to spins located under the central part of the wire. Since the aluminium wire is superconducting, the current density is higher on the edge of the wire than in the central part, and spins at $B_0 = 2.6$ mT are

thus more strongly coupled to the resonator than spins at $B_0 = 2.8$ mT. To estimate the difference in g, we measure the spin relaxation time T_1. As T_1 is radiatively limited by the Purcell effect in our experiment [9], we have $T_1^{-1} = 4g^2/\kappa$. Measuring T_1 at $B_0 = 2.6$ mT and $B_0 = 2.8$ mT (see Fig. S3a) and assuming that only the central value g_0 of the spin distribution should be adjusted, we determine $g_0^{(2.6\ \mathrm{mT})}/2\pi = 93$ Hz.

We next adjust the distributions overall weighting factor N_D until we are able to reproduce the difference in the echo amplitudes recorded at $B_0 = 2.6$ mT and $B_0 = 2.8$ mT (see Fig. S3b). We find $N_D = 1.4 \times 10^4$ and thus infer the number of excited spins to be $N_{\mathrm{spins}} = 4.7 \times 10^3$.

Finally, we determine the sensitivity N_{min} defined in the main text as the minimum number of spins detectable per echo with a SNR of 1. In the data shown in Fig. 5c of the main text, the single-shot SNR is 0.37 in the absence of squeezing and we hence have $N_{\mathrm{min}} = N_{\mathrm{spins}}/SNR = 1.3 \times 10^4$. This larger value compared to [4] is due to the lower quality factor of the resonator.

Thanks to these numerical simulations, we can also check the assumptions of low cooperativity made in Section II of the main text. Using the model corresponding to $B_0 = 2.6$ mT, we find $C(0) = 0.002$, verifying $C(0) \ll 1$ and thus confirming that the spin-noise contribution can be neglected at low squeezing.

III. CHARACTERIZATION OF THE MEAN NUMBER OF THERMAL PHOTONS

In order to produce a squeezed vacuum state of the field $\hat{b}_{\mathrm{in}}$ that serves as input to the ESR resonator, the squeezer "SQZ" is pumped while its input is in the vacuum state (see Fig. S1). However, due to imperfect filtering of the microwave probe lines and to the refrigerator finite base temperature, one can never reach perfect electromagnetic vacuum. In this section, we describe the calibration procedure used to place an upper bound on the average excitation number of the input Fourier modes $\tilde{b}_{\mathrm{in}}(\omega)$ around the ESR resonator resonance frequency (typically $|\omega - \omega_0| \leqslant \kappa_c$) when the squeezer is off. Note that this average excitation number is in fact characterized at a slightly different frequency $\omega_1/2\pi = 7.62$ GHz, but we assume that the thermal equilibrium is similar so that $\langle \tilde{b}_{\mathrm{in}}^\dagger(\omega)\tilde{b}_{\mathrm{in}}(\omega)\rangle = \langle \tilde{b}_{\mathrm{in}}^\dagger(\omega_1)\tilde{b}_{\mathrm{in}}(\omega_1)\rangle$ for all relevant values of ω. This assumption is reasonable given that $|\omega - \omega_1| \ll k_B T$ (T being either the

refrigerator base temperature, or the effective temperature of the modes given at the end of this section), and that the transmission of the microwave input lines is flat (±0.5 dB) variation) on this frequency range.

The method consists in replacing, in a subsequent cool-down of the refrigerator, the ESR resonator with a transmon superconducting qubit [10] coupled to a microwave readout resonator with resonance frequency ω_1. The resonator-qubit system is in the so-called *strong dispersive regime* of circuit QED in which photons in the resonator mode lead to dephasing of the qubit [11, 12]. Thus, by measuring the dephasing rate of the qubit beyond the effect of population relaxation $\gamma_\phi = \gamma_2 - \gamma_1/2$, one can place an upper bound on the thermal photon number in the readout resonator, and then on the occupation of the travelling modes $\hat{b}_{\rm in}$.

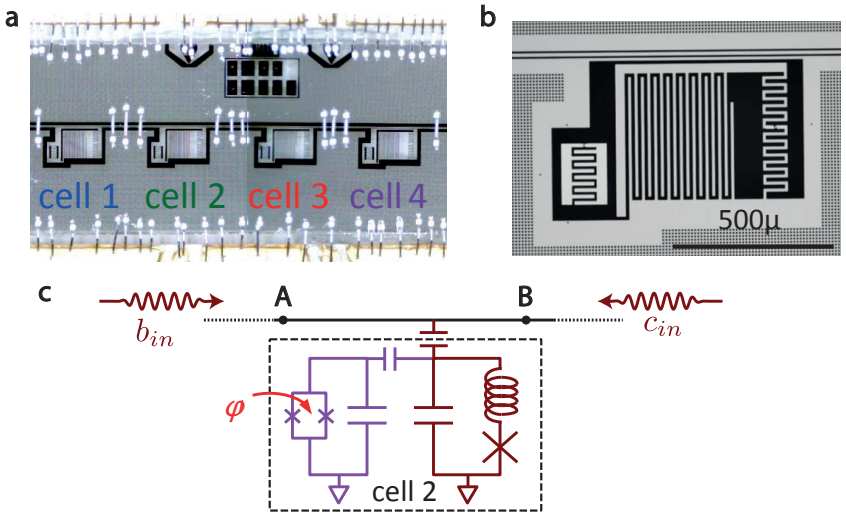

FIG. S4. **a)** Optical micrograph of the device used for estimating the number of thermally excited photons in $\hat{b}_{\rm in}$. Four cells, each one composed of a transmon qubit with an attached readout resonator are probed with a single microwave feedline. **b)** Zoom on one of the cells, showing the tunable transmon qubit (to the left) capacitively coupled to the readout resonator (to the right), itself capacitively coupled to the feedline (to the top). **c)** Simplified electric circuit of the cell used for the calibration. The qubit contains a split Josephson junction and its resonance frequency can be tuned by threading the loop with a magnetic flux φ. The resonator, which contains an array of junctions, is slightly non-linear. Thermal excitations in the resonator are due to both right and left travelling modes $\hat{b}_{\rm in}$ and $\hat{c}_{\rm in}$ in the feed line.

The device that we use was not designed specifically for the experiment, but was studied

in Ref. [13]. On a sapphire chip, 4 lumped element microwave readout resonators, each one capacitively coupled to a transmon qubit (see Fig. S4), are coupled to a single transmission feed line. In the following, we consider only the qubit-resonator system labeled *cell 2* (the other ones are well out of resonance). The feed line is connected to the setup depicted on Fig. S1 at points A and B. Note that in this geometry, the readout resonator thermal occupation is set by the average occupation of right propagating modes $\hat{b}_{\text{in}}$ through A and left propagating modes $\hat{c}_{\text{in}}$ through B (see Fig. S4 a). Internal losses of the readout resonator, that could act as a coupling to a fictitious cold reservoir, are shown to be negligible on Fig. S6 d. The blue input line connected at B on Fig. S1, which was originally designed to probe the ESR resonator in reflection on port 1, is less attenuated by 10 dB than the green line connected to A so that left propagating modes tend to increase the thermal occupation of the readout resonator. This issue does not arise with the ESR resonator since the coupling rate through port 1 is negligible ($\kappa_1 \ll \kappa_2$). Thus, the calibration made here is conservative and the estimation of the thermal occupation of $\hat{b}_{\text{in}}$ is an upper bound of the actual value in the experiment.

The readout resonator consists of an interdigitated capacitor made out of superconducting aluminum in parallel with an array of Josephson junctions (Fig. S4). This array behaves as a non-linear inductor and was originally designed for single-shot readout of the attached qubit. This non-linearity is not relevant here and can be neglected as the average photon number in the resonator is well below one. The transmon qubit is made out of a smaller interdigitated capacitor in parallel with a split Josephson junction that allows to tune its resonance frequency. A DC magnetic field is then applied using a superconducting coil in order to operate the device at its *sweet spot*, where its frequency $\omega_q/2\pi = 6.23$ GHz does not depend on the magnetic field fluctuations to first order (see Fig. S5).

The coupling rate of the qubit and readout resonator is much smaller than the detuning $\omega_1 - \omega_q$ so the system is described by the dispersive hamiltonian [12]

$$\hat{H} = \hbar\omega_1(\hat{a}^\dagger\hat{a} + \frac{1}{2}) + \hbar\omega_q\frac{\hat{\sigma}_z}{2} + \hbar\chi\hat{a}^\dagger\hat{a}\hat{\sigma}_z. \tag{S15}$$

Here, $\hat{\sigma}_z$ is the Pauli operator of the qubit and χ is the qubit state dependent shift of the readout resonator frequency, which provides us with a robust readout method of the transmon [14, 15]. Indeed, by probing the resonator with a near resonant microwave field and integrating a quadrature of the transmitted field, one gets a signal $\overline{S}$ depending linearly

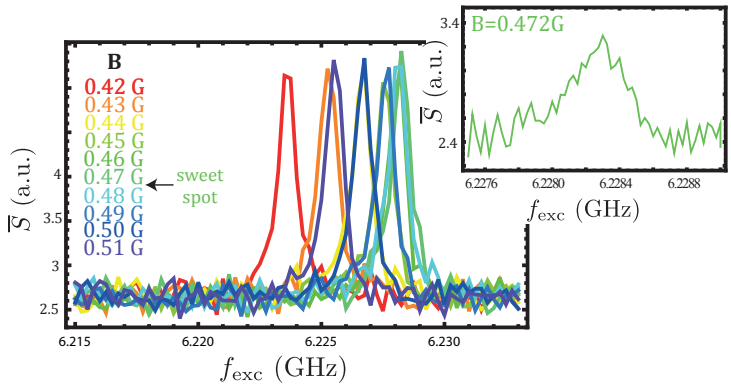

FIG. S5. **Two-tone spectroscopy** of the qubit. Starting from thermal equilibrium, the qubit is excited by a 5 μs-long saturating pulse (power -20 dBm referenced at refrigerator input) of frequency f_{exc} and then readout with an optimized pulse around $\omega_1/2\pi$ (see text and Fig. S6). The integrated signal $\overline{S}$ reveals the qubit excited state occupation. One can vary the qubit resonance frequency by varying the amplitude of the applied B-field (encoded in color). **Inset:** desaturated qubit resonance (power -30 dBm at fridge input) at the sweet spot, showing that $\omega_q/2\pi = 6.228$ GHz.

on $\langle\sigma_z\rangle$. In practice, the power, duration and frequency of the readout pulse was empirically adjusted to optimize signal-to-noise ratio. It corresponds to few photons in the resonator (power 10 dB larger than for 1 photon characterization of the resonator on Fig S6 d). Note that the amplifier JPA was turned off during all measurements.

In Ref. [16], Rigetti *et al.* computed the dephasing rate of a qubit induced by thermally excited photons in the readout resonator mode. It reads

$$\gamma_{\rm phot} = \frac{\kappa}{2}\mathrm{Re}\left\{\sqrt{\left(1+2i\frac{\chi}{\kappa}\right)^2 + 8i\overline{n}\frac{\chi}{\kappa}} - 1\right\}, \tag{S16}$$

where κ is the photon exit rate from the readout resonator and $\overline{n} = \langle\hat{a}^\dagger\hat{a}\rangle$ is the mean number of photons hosted by the resonator. Considering that $\gamma_{\rm phot} \leq \gamma_\phi = \gamma_2 - \gamma_1/2$, we now measure the qubit population and coherence relaxation rates γ_1 and γ_2 as well as all parameters entering the expression S16 in order to place an upper bound on $\overline{n}$.

By applying π and $\pi/2$ excitation pulses (calibrated by recording Rabi oscillations of the qubit), we first measure the qubit population relaxation rate $\gamma_1 = 0.41$ μs^{-1} (see Fig. S6 a) and coherence relaxation rate $\gamma_2^* = 1.1$ μs^{-1} (see Fig. S6 b). This last rate corresponds to a free-induction decay measurement, and includes the effect of low-frequency noise, such as second order effects of the fluctuations in the flux threading the qubit loop, along with

high-frequency noise induced by thermal photons in the readout resonator. A Hahn-echo measurement, yielding a decay rate $\gamma_{2,\text{echo}} \simeq \gamma_2^*$ shows that the former is negligible compared to the latter (see Fig. S6 c). We can then extract the qubit pure dephasing rate $\gamma_\phi = \gamma_2 - \gamma_1/2 = 0.9\ \mu\text{s}^{-1}$.

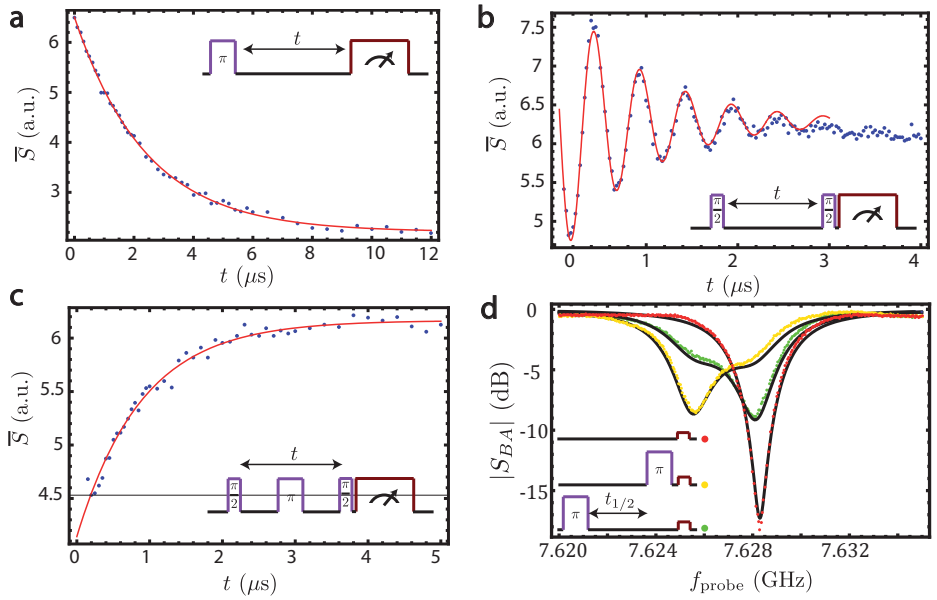

FIG. S6. **Qubit-resonator parameters characterization**. For each measurement, the pulse sequence is schematically represented at ω_q (in purple, all rotations around σ_y of the qubit) and at $\omega_{\text{readout}} \simeq \omega_1$ (in brown). **a)** Population relaxation measurement yielding $T_1 = 2.4\ \mu$s, **b**) Free induction decay measurement yielding $T_2^* = 0.9\ \mu$s (excitation pulses at $\omega_q/2\pi + 2$ MHz). **c)** Hahn-echo measurement yielding $T_{2,\text{echo}} = 0.9\ \mu$s. **d)** Measured transmission coefficient S_{AB} when the qubit is at thermal equilibrium (red dots), right after an inverting π-pulse (yellow dots) and a qubit half-life after a π-pulse (green dots). Black lines: global fit with parameters $p_\pi = 0.66$, $\chi/2\pi = 1.48$ MHz and $\kappa_{\text{int}}/\kappa_{\text{ext}} = 0.14$. For **a**, **b** and **c** the readout pulse power is empirically adjusted to optimize signal to noise ratio and the transmitted field is integrated over 5 μs. Only the quadrature $\overline{S}$ containing information on the qubit state is plotted. For **d** the readout pulse power is low enough that readout resonator non-linearity is neglected and the transmitted field is integrated over 0.2 μs in the stationary regime.

In order to measure χ, we then detect the transmitted signal through the feed line for a probe pulse of low amplitude (linear regime of the readout resonator) and integrate the signal over 0.2 $\mu\text{s} \ll T_1$ in the stationary regime of the resonator (signal during ring-up is

discarded in order to avoid distortion of the signal). The transmission coefficient from A to B then reads [17]

$$S_{BA}(\omega) = p\frac{\kappa_{\text{int}} + 2i(\omega - \omega_{\text{res}} - \chi)}{\kappa_{\text{int}} + \kappa_{\text{ext}} + 2i(\omega - \omega_{\text{res}} - \chi)} + (1-p)\frac{\kappa_{\text{int}} + 2i(\omega - \omega_{\text{res}} + \chi)}{\kappa_{\text{int}} + \kappa_{\text{ext}} + 2i(\omega - \omega_{\text{res}} + \chi)}, \quad \text{(S17)}$$

where κ_{ext} (resp. κ_{int}) is the resonator photon exit rate into the feed line (resp. due to internal losses) and $p = \langle 1 - \hat{\sigma}_z \rangle/2$ is the occupation of the ground state of the qubit. Note that the total photon exit rate from the resonator $\kappa = \kappa_{\text{int}} + \kappa_{\text{ext}} = 2.04 \times 10^7 \text{s}^{-1}$ is determined independently by measuring the ringdown time of the resonator.

We record this transmission coefficient at three different points: i) at thermal equilibrium ($p \simeq 1$, red dots on Fig. S6 d), ii) right after applying an inverting π-pulse ($p = p_\pi$, yellow dots) and, iii) for better precision, a duration $t_{1/2} = \ln(2)T_1$ after a π-pulse ($p = p_\pi/2$, green dots). If p_π can be roughly estimated given the drive pulse duration and delay before signal integration, it is difficult to predict accurately its value due to the reduction of T_1 in presence of a field in the readout resonator [18]. We rather estimate it along with the other parameters entering Eq. S17 by fitting these three curves altogether (black curves), which yields $p_\pi = 0.66$, $\chi/2\pi = 1.48$ MHz and $\kappa_{\text{int}}/\kappa_{\text{ext}} = 0.14$. In this fit, we allow for a global scaling factor accounting for the attenuation in the lines, and a small offset in the transmitted field complex amplitude, attributed to impedance mismatch.

From this calibration and using Eq. S16, we find for the readout resonator $\overline{n} \leq 0.1$. As mentioned in the beginning of this section, it is a conservative estimate of the average thermal photon number in the ESR resonator mode when the squeezer is off.

For a thermal state of a harmonic oscillator inside the ESR resonator when the squeezer is off, the fluctuations on one quadrature read

$$\delta X^2_{\text{off}} = \frac{\overline{n}}{2} + \frac{1}{4}. \quad \text{(S18)}$$

In the experiment, as seen in Figs. 3b,c of the main text, the detected output noise is reduced by a factor $\delta I^2_{\text{on}}/\delta I^2_{\text{off}} = 0.75$ when the squeezer is on. Due to background noise in the transmission channels, this represents an upper bound on the reduction in the fluctuations of the squeezed quadrature inside the ESR resonator, $\delta X^2_{\text{on}}\ /\delta X^2_{\text{off}} < 0.75$. With a thermal occupation of less than 0.1 photons inside the resonator, Eq. (S18) hence yields an upper bound on δX^2_{on},

$$\delta X^2_{\text{on}} < 0.75\left(\frac{\overline{n}}{2} + \frac{1}{4}\right) < 0.225, \quad \text{(S19)}$$

showing that the fluctuations are indeed reduced below the vacuum level ($\delta X^2_{\rm vac} = 1/4$).

The background noise contribution can be estimated when both SQZ and AMP are switched off. This allows the statement of a more stringent condition $\delta X^2_{\rm on}/\delta X^2_{\rm off} < \frac{\delta I^2_{\rm on} - \delta I^2_{\rm bg}}{\delta I^2_{\rm off} - \delta I^2_{\rm bg}} = 0.66$, (see Figs. 3b,c), which corresponds to a reduction of -1 dB below the vacuum fluctuations for the squeezed quadrature.

[1] C. W. Gardiner and P. Zoller, Quantum Noise, 2nd ed. (Springer, Berlin, 2000).

[2] Carlton M. Caves, "Quantum-mechanical noise in an interferometer," Phys. Rev. D **23**, 1693–1708 (1981).

[3] See main text.

[4] A Bienfait, J.J. Pla, Y. Kubo, M. Stern, X. Zhou, C.-C. Lo, C.D. Weis, T. Schenkel, M.L.W. Thewalt, D. Vion, D. Esteve, B. Julsgaard, K. Moelmer, J.J.L. Morton, and P. Bertet, "Reaching the quantum limit of sensitivity in electron spin resonance," Nature Nanotechnology **11**, 253 – 257 (2015).

[5] A. Palacios-Laloy, Superconducting qubit in a resonator : test of the Leggett-Garg inequality and single-shot readout, Ph.D. thesis, Universit´ Pierre-et-Marie-Curie (2010).

[6] X. Zhou, V. Schmitt, P. Bertet, D. Vion, W. Wustmann, V. Shumeiko, and D. Esteve, "High-gain weakly nonlinear flux-modulated josephson parametric amplifier using a squid array," Phys. Rev. B **89**, 214517 (2014).

[7] C. Grezes, B. Julsgaard, Y. Kubo, M. Stern, T. Umeda, J. Isoya, H. Sumiya, S. Abe, S. Onoda, T. Ohshima, V. Jacques, J. Esteve, D. Vion, D. Esteve, K. Moelmer, and P. Bertet, "Multimode storage and retrieval of microwave fields in a spin ensemble," Phys. Rev. X **4**, 021049 (2014).

[8] J. J. Pla, A. Bienfait, G. Pica, J. Mansir, F. A. Mohiyaddin, A. Morello, T. Schenkel, B. W. Lovett, J. J. L. Morton, and P. Bertet, "Strain-induced nuclear quadrupole splittings in silicon devices," .

[9] A. Bienfait, J.J. Pla, Y. Kubo, X. Zhou, M. Stern, C.-C. Lo, C.D. Weis, T. Schenkel, D Vion, D. Esteve, J.J.L. Morton, and P. Bertet, "Controlling spin relaxation with a cavity," Nature **531**, 74 – 77 (2016).

[10] Jens Koch, M Yu Terri, Jay Gambetta, Andrew A Houck, DI Schuster, J Majer, Alexandre Blais, Michel H Devoret, Steven M Girvin, and Robert J Schoelkopf, "Charge-insensitive qubit design derived from the cooper pair box," Physical Review A **76**, 042319 (2007).

[11] Jay Gambetta, Alexandre Blais, David I Schuster, Andreas Wallraff, L Frunzio, J Majer, Michel H Devoret, Steven M Girvin, and Robert J Schoelkopf, "Qubit-photon interactions in a cavity: Measurement-induced dephasing and number splitting," Physical Review A **74**,

042318 (2006).

[12] Alexandre Blais, Jay Gambetta, A Wallraff, DI Schuster, SM Girvin, MH Devoret, and RJ Schoelkopf, "Quantum-information processing with circuit quantum electrodynamics," Physical Review A **75**, 032329 (2007).

[13] Vivien Schmitt, X Zhou, K Juliusson, B Royer, Alexandre Blais, Patrice Bertet, Denis Vion, and D Esteve, "Multiplexed readout of transmon qubits with josephson bifurcation amplifiers," Physical Review A **90**, 062333 (2014).

[14] A Wallraff, DI Schuster, A Blais, L Frunzio, J Majer, MH Devoret, SM Girvin, and RJ Schoelkopf, "Approaching unit visibility for control of a superconducting qubit with dispersive readout," Physical review letters **95**, 060501 (2005).

[15] MD Reed, L DiCarlo, BR Johnson, L Sun, DI Schuster, L Frunzio, and RJ Schoelkopf, "High-fidelity readout in circuit quantum electrodynamics using the jaynes-cummings nonlinearity," Physical review letters **105**, 173601 (2010).

[16] Chad Rigetti, Jay M Gambetta, Stefano Poletto, BLT Plourde, Jerry M Chow, AD Córcoles, John A Smolin, Seth T Merkel, JR Rozen, George A Keefe, et al., "Superconducting qubit in a waveguide cavity with a coherence time approaching 0.1 ms," Physical Review B **86**, 100506 (2012).

[17] David M Pozar, Microwave engineering (John Wiley & Sons, 2009).

[18] Maxime Boissonneault, Jay M Gambetta, and Alexandre Blais, "Dispersive regime of circuit qed: Photon-dependent qubit dephasing and relaxation rates," Physical Review A **79**, 013819 (2009).